

Localized Anisotropic Subduction-Zone Structure in Southern Peru: Constraints from Teleseismic Receiver Functions and Forward Modeling

by Hyunsun Kang and YoungHee Kim

ABSTRACT

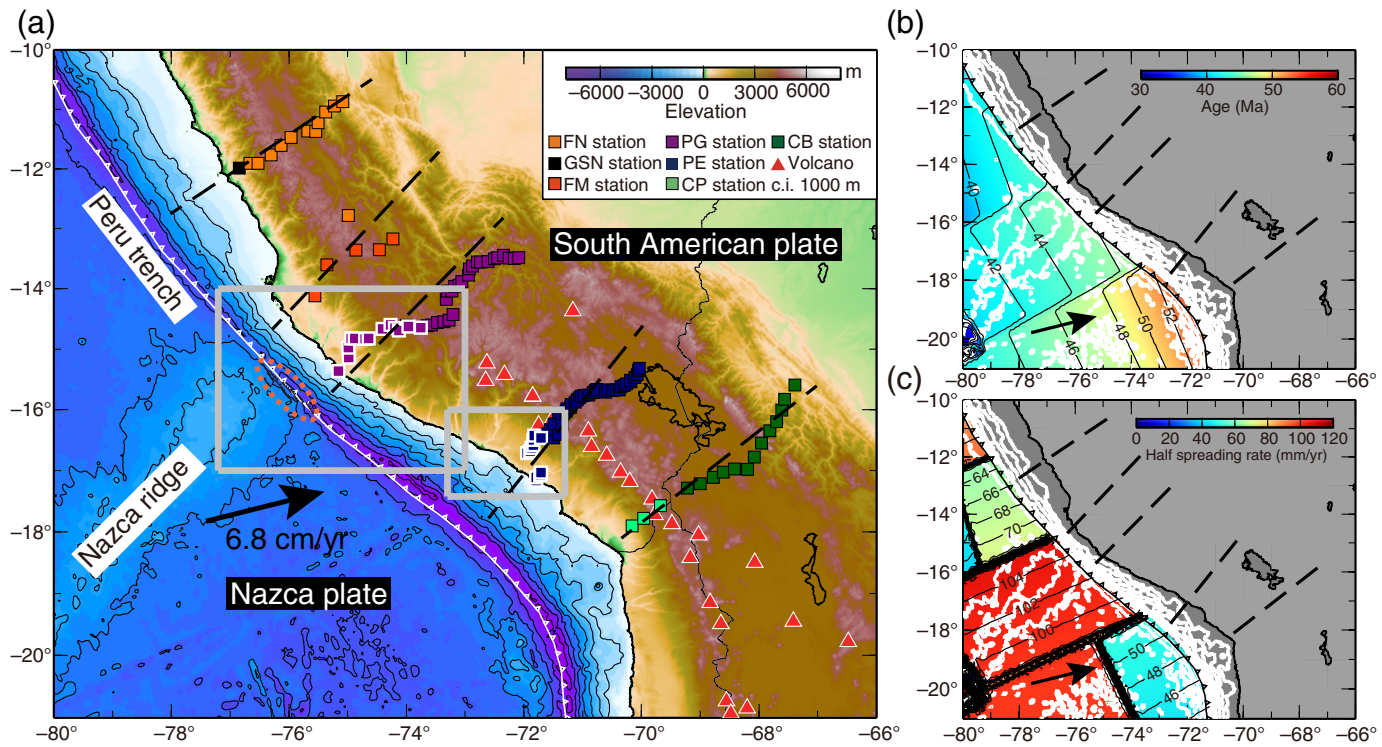
Significant subduction-zone complexity in southern Peru has been attributed to the subducting Nazca ridge. In this study, we constrained the seismic structure of the Nazca plate to the region where the ridge is subducting and its plate geometry transitions from flat to normal. We applied harmonic decomposition of teleseismic receiver functions (RFs) to retrieve isotropic and anisotropic structures of the oceanic crust and uppermost mantle of the plate, and provide model parameters that best represent the observed structures and clarify the geodynamic processes associated with plate subduction. Harmonic decomposition of the RFs revealed enhanced positive-polarity amplitudes for the dipping oceanic Moho, indicating the presence of a strong anisotropic (10%–20%) layer near/at the oceanic Moho. This condition requires either anisotropic oceanic crust (AOC) or anisotropic mantle lid (AML) with a predominant trench-normal fast axis of symmetry for the dipping segment of the slab. The seismic anisotropy produced by the AOC model may indicate strong crystal-preferred orientation of minerals within the oceanic crust or/and hydrous minerals associated with outer-rise faulting that developed prior to subduction. The presence of AML may point to frozen olivine fabric in the uppermost mantle of the slab, in alignment with the direction of paleoplate spreading. In the flat-slab region, the fast-axis orientation changes abruptly from trench-normal in the dipping segment to a random direction in the flat segment of the slab. Such disrupted patterns in the fast axes indicate slab fabric deformation due to a high degree of tectonic coupling between the two plates in response to subduction of the Nazca ridge and/or a change in slab dip during the slab-flattening process. Toward the southeast in the normal dip-slab region, the presence of frozen olivine fabric in AML is less evident, suggesting that fossil fabric may be overprinted by earlier tectonic processes.

Supplemental Content: Tables providing detailed information on the stations and model parameters used in this study, figures

showing maps of the distributions of teleseismic earthquakes and selected stations for receiver function (RF) modeling, determination of α_{\max} for those stations, harmonic decomposition of RFs, and synthetic test results for various models including two with a ultra-slow layer (USL), and animated movies showing 3D views of an anisotropic structure with a fast-axis trend and plunge for anisotropic mantle lid (AML) and anisotropic oceanic crust (AOC) models.

INTRODUCTION

The Nazca plate subduction zone is an excellent natural laboratory for examining along-arc variations in subduction-zone seismic properties and processes in southern Peru. Along the South American margin between 12° and 20° S latitude, the Nazca plate is a relatively young (about 42–52 Ma from northwest to southeast) oceanic plate, subducting at convergence rates of 6.8 cm/yr (Norabuena *et al.*, 1998), and this region involves slab-dip variability along the margin (Lim *et al.*, 2018, and references therein). In addition to changes in slab dip, significant subduction-zone complexity has arisen in response to the subduction of the Nazca ridge (Fig. 1), which has been migrating southward along the plate margin since about 11 Ma (Hampel, 2002). The present location of the Nazca ridge coincides with the southern end of the flat subduction segment (Hampel, 2002), where temporary broadband seismic arrays occur. Several arrays have broadly covered the flat-to-normal subduction zone for 1000 km along the arc (Fig. 1); such array datasets resulted in improved knowledge of the fore-arc structures and insight into earthquake rupture characteristics (Kim and Clayton, 2015), upper-plate seismic structure (Ryan *et al.*, 2016), and slab seismic structure (Phillips *et al.*, 2012; Phillips and Clayton, 2014; Dougherty and Clayton, 2015; Ma and Clayton, 2015; Scire *et al.*, 2015; Kumar *et al.*, 2016; Ward *et al.*, 2016; Bishop *et al.*, 2017; Lim *et al.*, 2018).



▲ Figure 1. Maps showing our study region in the Peruvian subduction zone. (a) Topographic–bathymetric map. The contour interval for bathymetry is 1000 m. Five trench-perpendicular profiles for the receiver functions (RFs) are shown as black dashed lines. All stations (squares) were used to constrain overall subduction-zone structures; a subset of the stations (PG01–PG22 and PE03–PE13; white-outlined squares) were used for RF modeling to constrain anisotropic structures. See [Figure S2](#) (available in the supplemental content to this article) for a zoomed-in map of station locations. The 119 temporary broadband seismic stations from the [Peru Subduction Experiment \(PeruSE, 2013; PE and PG lines\)](#), Peru Lithosphere and Slab Experiment (FN and FM lines; [Wagner et al., 2010](#)), Central Andean Uplift and Geodynamics of High Topography (CB and CP lines; [Beck et al., 2010](#)), and one permanent Global Seismographic Network station (NNA) are plotted. Relative plate motion of the Nazca plate (arrow with convergence rate) was obtained from [Norabuena et al. \(1998\)](#). The area enclosed by an orange dotted line contains normal faults striking parallel to the trench ([Hampel et al., 2004](#)). See Figure 7 for a zoomed-in map of fault locations. Gray boxes indicate regions shown in Figure 7. (b,c) Age and half-spreading rate of the subducting Nazca plate ([Müller et al., 2008](#)). The color version of this figure is available only in the electronic edition.

Subduction-zone seismic anisotropy is a key parameter that helped unravel complex geodynamic processes caused by interactions between two plates. The dense array data collected in southern Peru can provide further constraints on the nature of the slab-dip transition. Recent studies utilizing these array data have reported continental-scale seismic anisotropy beneath southern Peru from shear-wave splitting measurements ([Eakin and Long, 2013; Eakin et al., 2014; Eakin, Long, Scire, et al., 2015; Eakin, Long, Wagner, et al., 2015](#)). These studies reported a sharp transition in the splitting pattern with respect to the Nazca ridge axis, suggesting that the ridge indeed plays an important role in subduction-zone dynamics and mantle flow in the flat-slab system. From the multiple-phase splitting data, [Eakin and Long \(2013\)](#) observed a change in fast-splitting axes in the subslab mantle from trench-normal (in the northwest) to trench-oblique (in the southeast) with respect to the ridge axis. [Eakin et al. \(2014\)](#) observed trench-parallel fast axes in the mantle wedge between the flat slab and the upper plate in the north of the ridge from local *S*-splitting measurements, and suggested that the mantle wedge had been

deformed by trench-parallel shearing during the passage of the ridge. [Eakin, Long, Scire, et al. \(2015\)](#) observed the northwest–southeast (along-strike) fast axis of the Nazca slab (at a depth of 200–400 km) from local *S* data, and suggested that the fossilized slab fabric had been overprinted by along-strike extension during slab flattening. Furthermore, [Eakin, Long, Wagner, et al. \(2015\)](#) used SKS splitting data as evidence that complex and multilayered anisotropy within the upper mantle was related to ridge subduction. In addition, [Antonijevic et al. \(2016\)](#) utilized the Rayleigh-wave phase constraints to suggest an alteration of the slab petrofabric in the southern part of the ridge, and preservation of the primary (fossilized) fabric in the northern part. A recent study utilized teleseismic receiver functions (RFs) to reveal evidence of multilayered anisotropy within the crust and uppermost mantle beneath the Peruvian flat-slab region (north of the Nazca ridge axis) and the normal dip-slab region in northern Bolivia ([Bar et al., 2019](#)).

In this study, we examined teleseismic *P*-to-*S*-converted phases recorded by the [Peru Subduction Experiment \(PeruSE, 2013\)](#), Peru Lithosphere and Slab Experiment (PULSE;

Wagner *et al.*, 2010), Central Andes Uplift and Geophysics of High Topography experiment (CAUGHT; Beck *et al.*, 2010), and one permanent Global Seismographic Network (GSN) station to identify fine-scale isotropic and anisotropic structures and provide a key constraint on the style of deformation near the plate boundary in the region where slab geometry is changing from flat to normal (Fig. 1). Teleseismic *P*-to-*S*-converted phases (or RFs) provide enhanced sensitivity at localized velocity gradients across lithospheric discontinuities, and are therefore particularly useful for resolving kilometer-scale seismic anisotropy structure (e.g., Song and Kim, 2012a,b; Audet, 2013). We provide a more complex model of seismic anisotropy (plunging axis of hexagonal symmetry) than depth-integrated measurements such as *SKS* splitting and surface-wave dispersion. Using a combination of RF harmonic decomposition and synthetic forward modeling, we provide candidate models that include the effects of structural heterogeneity and anisotropy, and discuss deformation style caused by interactions between the Nazca and overriding plates, and also with the Nazca ridge in southern Peru.

DATA AND METHODS

Data Analysis

We collected teleseismic earthquake data recorded at 119 temporary seismic stations by the PeruSE (2013), Peru Lithosphere and Slab Experiment (PULSE, Wagner *et al.*, 2010), and Central Andes Uplift and Geophysics of High Topography (CAUGHT, Beck *et al.*, 2010), and one permanent Global Seismographic Network (GSN) station (Fig. 1; \ominus Table S1, available in the supplemental content to this article). Of the collected earthquake data, we selected only events from a teleseismic distance range for *P* waves (30° – 95°) with magnitude > 5.5 for all available back azimuths. We then visually inspected the *P*-wave phase for all waveforms, and selected those with a clear arrival. A total of 350 events passed quality checks within a station operation period of ≤ 5 yr (\ominus Table S1); the back-azimuthal distribution of these events is roughly complete (Fig. 2). Waveforms were filtered using a band-pass filter from 0.01 to 1.0 Hz, which is the same filter range used in a previous RF study (Kim and Clayton, 2015), and then windowed between 10 s before and 60 s after *P*-wave arrival.

RF Calculation

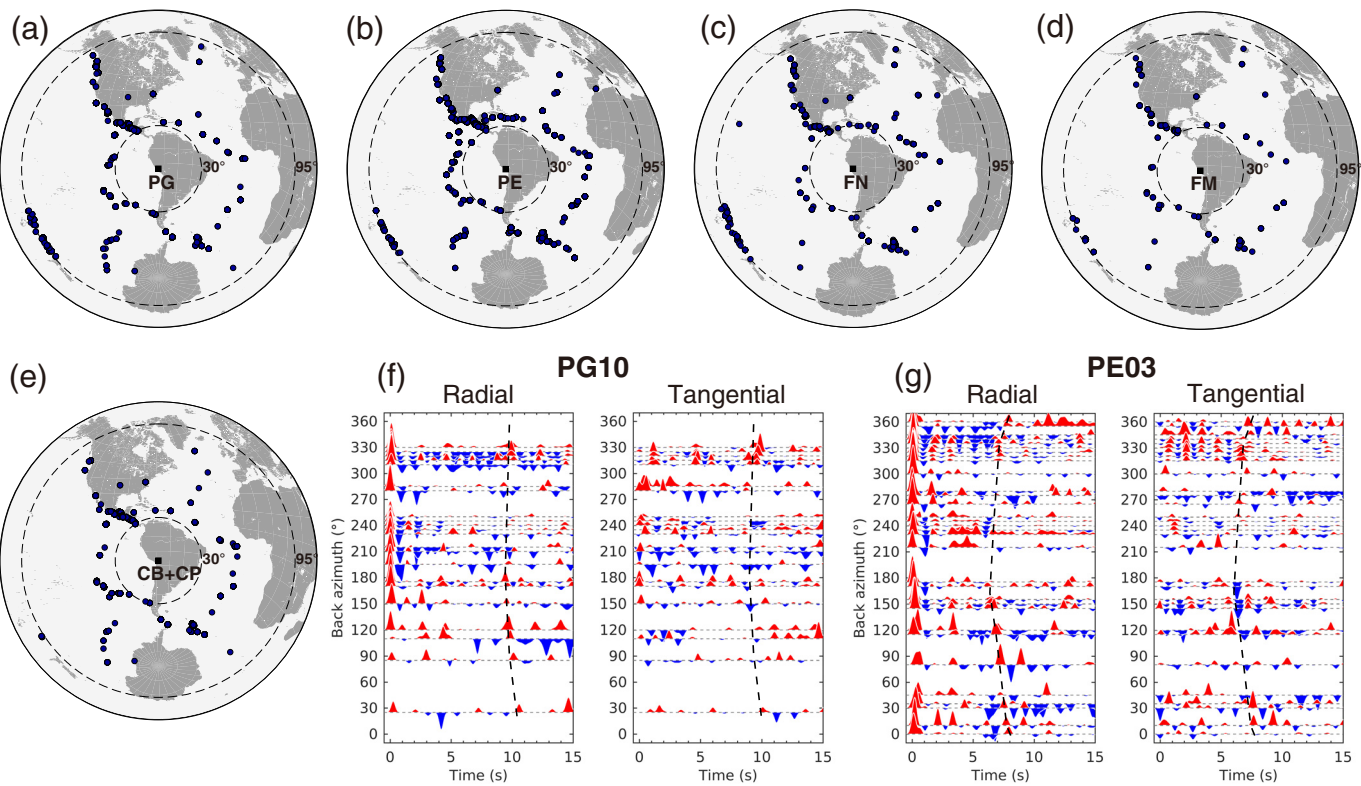
RF calculation involves two key steps: (1) coordinated rotation, which isolates the *P*-to-*S*-converted phase (Pds , in which d denotes discontinuity) from the incident *P* wave, and (2) deconvolution, which removes source and propagation path effects (Ammon, 1991; Rondenay, 2009). Three-component north–east–vertical (N–E–Z) data are rotated to a radial–tangential–vertical (R–T–Z) coordinate system. Following coordinate rotation, R- and T-component seismograms are deconvolved with the Z-component seismogram at each station to obtain R- and T-component RFs, respectively. Deconvolution is performed in the time domain (Ligorria and Ammon, 1999) with a Gaussian parameter of 4 and a maximum of 100 iterations. RFs are converted into a depth domain using the regional 1D velocity model of southern Peru (Lim *et al.*, 2018), and then stacked for all back azimuths to improve the signal-to-noise ratio of Pds phases.

RF Harmonic Decomposition

When a teleseismic *P* wave passes through an isotropic horizontal plane, the wave is converted to an *SV* wave; the converted *SV*-wave energy is then mapped onto R-RF. However, when a *P* wave passes through a dipping interface or anisotropic medium, the *P*-wave energy is scattered, generating an *SH* wave, which can be mapped onto T-RF. Thus, back-azimuthal variation in *SH*-wave energy in T-RF can provide information about the nature of the interface at the depth where the ray impinges. In particular, anisotropy with a horizontal symmetry axis produces a four-lobed RF amplitude pattern, whereas a dipping interface or a tilted symmetry axis produces a two-lobed pattern (Cassidy, 1992; Nagaya *et al.*, 2008; Park and Levin, 2016).

Both R- and T-RFs can be analyzed simultaneously by extracting the back-azimuthal harmonics of the RF dataset (Shiomi and Park, 2008; Bianchi *et al.*, 2010; Piana Agostinetti *et al.*, 2011; Piana Agostinetti and Miller, 2014). R- and T-RFs can be linearly regressed into five harmonic terms, as shown in equation (1) (Bianchi *et al.*, 2010; Audet, 2015; Liu *et al.*, 2015), and expressed as a sum of $\cos(k\phi)$ and $\sin(k\phi)$, in which k represents the harmonic degree or order ($k = 0, 1$, and 2) and ϕ represents the back azimuth.

$$\begin{bmatrix} R_1(z) \\ \vdots \\ R_N(z) \\ T_1(z) \\ \vdots \\ T_N(z) \end{bmatrix} = \begin{bmatrix} 1 & \cos(\phi_1 - \alpha) & \sin(\phi_1 - \alpha) & \cos(2(\phi_1 - \alpha)) & \sin(2(\phi_1 - \alpha)) \\ \vdots & \vdots & \vdots & \vdots & \vdots \\ 1 & \cos(\phi_N - \alpha) & \sin(\phi_N - \alpha) & \cos(2(\phi_N - \alpha)) & \sin(2(\phi_N - \alpha)) \\ 0 & \cos\left(\phi_1 - \alpha + \frac{\pi}{2}\right) & \sin\left(\phi_1 - \alpha + \frac{\pi}{2}\right) & \cos\left(2\left(\phi_1 - \alpha + \frac{\pi}{4}\right)\right) & \sin\left(2\left(\phi_1 - \alpha + \frac{\pi}{4}\right)\right) \\ \vdots & \vdots & \vdots & \vdots & \vdots \\ 0 & \cos\left(\phi_N - \alpha + \frac{\pi}{2}\right) & \sin\left(\phi_N - \alpha + \frac{\pi}{2}\right) & \cos\left(2\left(\phi_N - \alpha + \frac{\pi}{4}\right)\right) & \sin\left(2\left(\phi_N - \alpha + \frac{\pi}{4}\right)\right) \end{bmatrix} \begin{bmatrix} A(z) \\ B_{\parallel}(z) \\ B_{\perp}(z) \\ C_{\parallel}(z) \\ C_{\perp}(z) \end{bmatrix}, \quad (1)$$



▲ Figure 2. Maps showing teleseismic earthquakes for RF calculation and single-station RFs. Event distributions for the (a) PG, (b) PE, (c) FN, (d) FM, and (e) CB + CP lines are shown as navy blue dots. Epicentral distances of 30° and 95° from the central point of each array (black square) are marked as thin dashed lines. Event distributions for a subset of PG and PE lines for RF modeling are shown in □ Figure S1. Each station dataset included a minimum of 9 and maximum of 101 earthquakes. We ensured good back-azimuth distribution for the subset of stations used for RF modeling (□ Fig. S1). Each station dataset used for modeling included a minimum of 19 and maximum of 81 earthquakes. (f,g) Radial and tangential RFs of the PG10 and PE03 stations. RFs were stacked in 5° back-azimuth bins. Positive amplitudes (red) indicate increasing impedance with depth; negative amplitudes (blue) indicate decreasing impedance with depth. Black dashed lines represent Pds conversion at the oceanic Moho. The color version of this figure is available only in the electronic edition.

in which $R_i(z)$ and $T_i(z)$ correspond to depth (z)-converted R- and T-RFs, respectively, for $i = 1$ to N RFs, and ϕ_i and α represent the back azimuth of the i th RF and any azimuth of interest, respectively. $A(z)$, $B_{\parallel}(z)$, $B_{\perp}(z)$, $C_{\parallel}(z)$, and $C_{\perp}(z)$ are coefficients of the $\cos(k\phi)$ and $\sin(k\phi)$ terms.

The $A(z)$ term ($k = 0$ harmonics) is a constant term that indicates a lack of dependence of the RF amplitudes on ϕ , thus providing information on isotropic structure. The two $B(z)$ terms ($k = 1$ harmonics) are orthogonal harmonics that can be shown as a two-lobed pattern of amplitudes in ϕ , and provide a proxy to indicate the presence of either a dipping interface or an anisotropic medium with a plunging symmetry axis. The $C(z)$ terms ($k = 2$ harmonics) can be shown as a four-lobed pattern of amplitudes in ϕ , indicating an anisotropic layer with a horizontal symmetry axis. The anisotropy modeled in this study is composed of hexagonal symmetry and its symmetry axis, that is, a unique fast or slow symmetry axis and uniformly slow or fast velocities, respectively, for wave propagation directions in the plane perpendicular to that axis (Weiss *et al.*, 1999).

Equation (1) was first introduced by Bianchi *et al.* (2010) for the case when $\alpha = 0^{\circ}$; α was later implemented in the equation by Audet (2015). When $\alpha = 0^{\circ}$, a strong B_{\parallel} component indicates preferential north-south orientation in structural heterogeneities or/and anisotropy, whereas strong B_{\perp} indicates preferential east-west orientation (Bianchi *et al.*, 2010). By varying α , the B_{\parallel} , B_{\perp} , C_{\parallel} , and C_{\perp} components can be resolved onto any azimuth α . In theory, there exists a particular α at each depth that maximizes the energy on one harmonic component (i.e., B_{\perp}), while minimizing the energy on the other component (i.e., B_{\parallel}). We thus define α_{\max} as an azimuth that produces maximum positive amplitude of one harmonic term (i.e., B_{\perp}) at any depth of interest, which we denote Z_{α} . In this study, we focus on the depth of the base of the subducting oceanic crust (i.e., oceanic Moho) for Z_{α} , in which amplitudes at Z_{α} are large in both A and B_{\perp} , and also define α_{\max} as the azimuth that produces maximum positive amplitude of B_{\perp} at Z_{α} . The parameter α_{\max} provides the first-order information on subsurface structures because it has a clear geological relationship to the foliation or strike of an interface (Schulte-Pelkum and Mahan, 2014a,b).

Table 1
Values of α_{\max} and Z_α at Stations on the PG and PE Lines for Receiver Function (RF) Modeling

Station	α_{\max} (°)	Z_α (km)	Station	α_{\max} (°)	Z_α (km)
PG01	290	42.70	PE03	0	56.60
PG05	310	60.00	PE04	350	60.10
PG06	310	66.60	PE05	310	65.30
PG07	280	74.40	PE06	310	71.40
PG08	300	73.90	PE07	320	80.70
PG10	320	86.10	PE08	310	81.40
PG11	320	89.90	PE09	290	86.30
PG15	250	98.70	PE10	310	87.50
PG16	40	101.20	PE11	260	95.30
PG17	190	96.10	PE12	290	97.10
PG18	20	93.40	PE13	320	98.10
PG21	210	102.80			
PG22	330	105.10			

Synthetic Forward Modeling

We generated synthetic RFs using RAYSUM (Frederiksen and Bostock, 2000), a wave propagation code that incorporates both dipping and anisotropic structures. Each layer in the model is defined by geometrical quantities (layer thickness, strike, and dip; (Fig. S2–S4) and material properties (P - and S -wave velocities [V_P and V_S], density, and anisotropy). The parameters that characterize the anisotropic structure are anisotropy strength and trend (tr) and plunge (pl) of the anisotropic symmetry axis. We first investigated relationships among dipping or/and anisotropic structure, RFs, RF harmonic decomposition, and $\alpha_{\max}(z)$ for three simple cases (Fig. 3). We then explored more realistic geometry models based on previously proposed models for our study region (Phillips et al., 2012; Dougherty and Clayton, 2015; Lim et al., 2018) and other shallow subduction-zone fore-arcs (Song and Kim, 2012a; Audet, 2013; Fig. 4) to resolve anisotropic structures. Multiples were not considered in the model because they do not interfere with the estimated arrival time of the Pds phase from the oceanic Moho, which is our primary interest.

Three representative models for PG and PE stations (Fig. 4) include possible structural features near the oceanic Moho: (1) an isotropic model including only a dipping oceanic crust, (2) an anisotropic mantle lid (AML) model, and (3) an anisotropic oceanic crust (AOC) model. For all models, we used the 1D regional velocity model of Phillips et al. (2012) and the density model of Tassara et al. (2006). We assumed the strike of the slab to be the same as the strike of the Peru trench, and therefore used 315° and 310° for the PG and PE lines, respectively. Synthetic RFs were calculated using the same back-azimuth and slowness ranges as observed in the data. Anisotropy strength was tested for two values: 10% and 20%. The symmetry axis trend varied from 0° to 350° and plunge from 0° to 90°, in 10° increments. The anisotropic parameter η was set as 1.03, which is a RAYSUM default value (Frederiksen and Bostock,

2000). This parameter describes the shape of the velocity ellipsoid between the fast and slow axes of P -wave velocity (Porter et al., 2011).

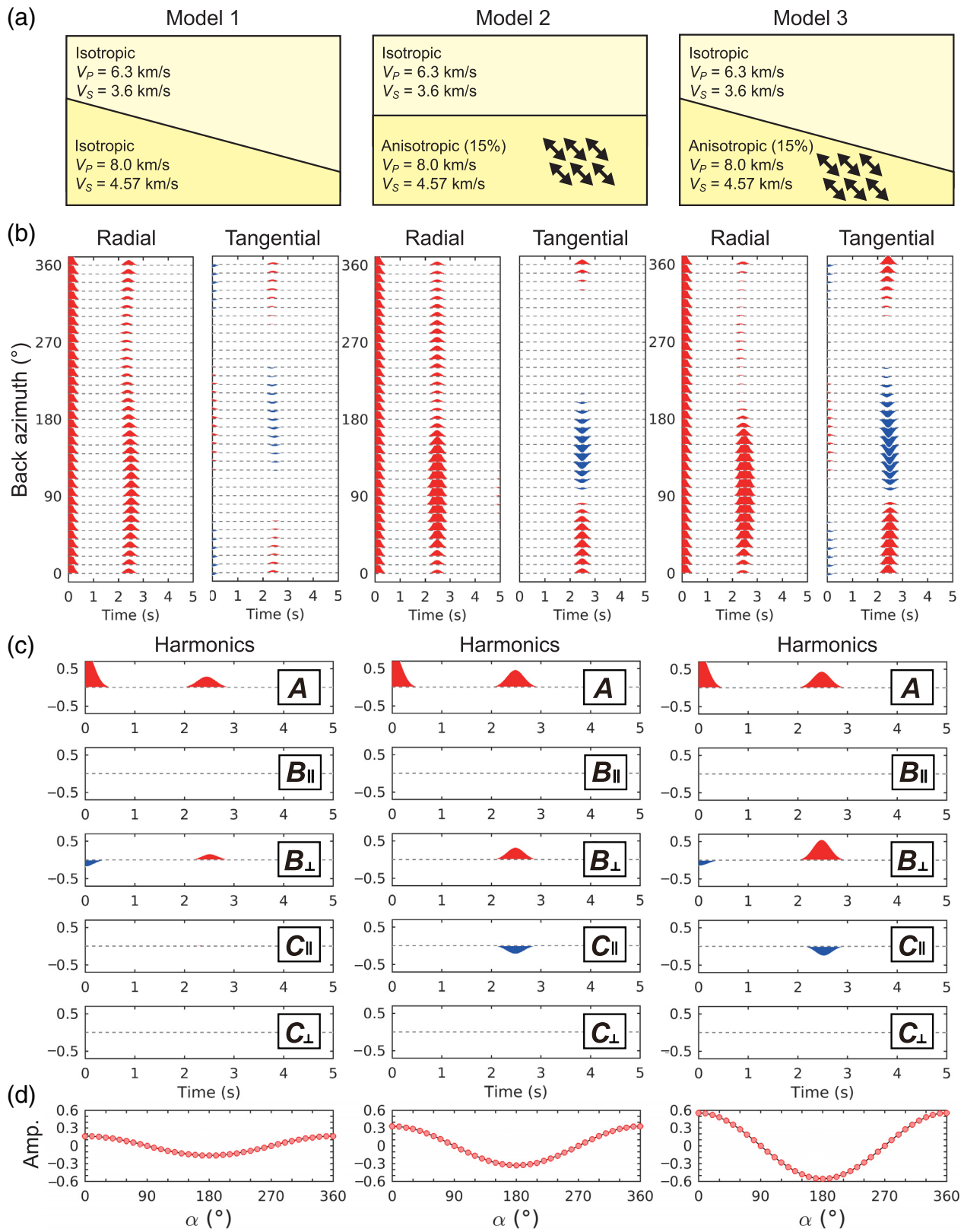
Harmonic decomposition was then applied to the synthetic RFs with previously determined α_{\max} values for each station (Table 1; (Fig. S3)). Synthetic and observed RF harmonics were compared by evaluating the root mean square misfit of A , B_\perp , and B_\parallel over a depth range of (positive) pulse widths of Pds from the oceanic Moho at the observed B_\perp at each station.

SYNTHETIC RF HARMONIC DECOMPOSITION: A SIMPLE MODEL EXAMPLE

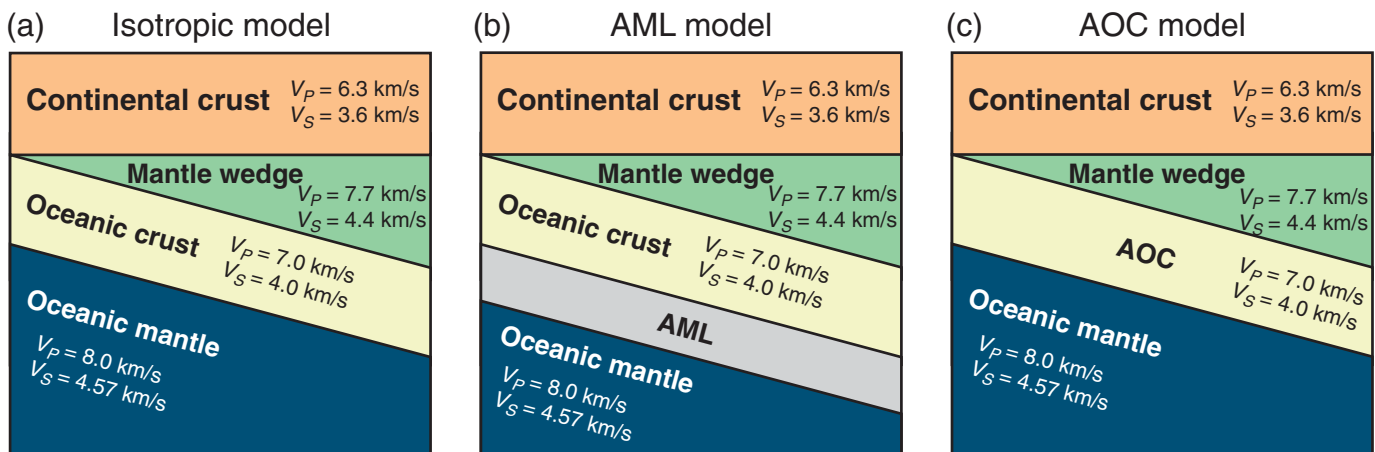
Figure 3b,c shows synthetic R- and T-RFs and corresponding harmonics for $\alpha = 0^\circ$ for three simple cases involving dipping or/and anisotropic structures (Fig. 3a). The model geometry was set as follows: model 1 includes a dipping isotropic interface with a strike of 0° and a dip of 15°; model 2 includes a horizontal interface and 15% anisotropy with tr = 90° and pl = 45° in the lower layer; and model 3 has both a dipping interface and anisotropy (as model 2) in the lower layer (Fig. 3a). We also explored another set of models in which the slower anisotropic layer is overlain on the faster isotropic layer ((Fig. S6).

Synthetic RFs for the three models (Fig. 3a) showed expected Pds conversion from the horizontal/dipping interface at about 2.5 s, indicating a delay following the direct P arrival at 0 s (Fig. 3b). T-RFs showed a two-lobed back-azimuth pattern with polarity flips at 90° and 270° (Fig. 3b). RF harmonics for $\alpha = 0^\circ$ showed positive B_\perp amplitude at 2.5 s and zero B_\parallel amplitude at 2.5 s (Fig. 3c). We tracked changes in B_\perp amplitude while changing α from 0° to 360°, and searched for an angle α_{\max} that would maximize the positive amplitude of B_\perp (Fig. 3d and (Fig. S6d). For all models (Fig. 3a and (Fig. S6a), α_{\max} was 0° (Fig. 3d and (Fig. S6d). We found that α_{\max} indicated a strike of the dipping interface in model 1 (Fig. 3a), and α_{\max} an orientation perpendicular to the fast-axis trend in the lower anisotropic layer (thus, tr = $\alpha_{\max} + 90^\circ$) in model 2 (Fig. 3a). When the slower anisotropic layer was overlain on the faster isotropic layer ((Fig. S6a), α_{\max} indicated an orientation perpendicular to the fast-axis trend of the anisotropic layer, but in an opposite direction from that of model 2 (Fig. 3a; thus, tr = $\alpha_{\max} - 90^\circ$).

Polarity flip points among the RFs changed with the strike of the dipping interface and the fast-axis trend of the anisotropic layer; thus, B_\perp amplitude changed with different α ((Fig. S7a). By design, both dipping and anisotropy produced the same polarity flip points in the two-lobed back-azimuth pattern, allowing us to obtain a maximum B_\perp amplitude (Fig. 3c and (Fig. S6c). In this case, α_{\max} indicates both tr ± 90° and the strike of the dipping interface. In cases where the anisotropy symmetry axis and dipping layer produce different flip points, α_{\max} may not follow either relationships ((Fig. S7b,c).



▲ **Figure 3.** Synthetic RFs and harmonic terms (A , B_{\parallel} , B_{\perp} , C_{\parallel} , and C_{\perp}) for three simple models. (a) Diagrams of the three models. The strike and dip of the dipping layer were set as 0° and 15° , respectively. The trend and plunge of the fast-symmetric axis of the anisotropic layer were set as 90° and 45° , respectively. (b) Synthetic radial and tangential RFs plotted as a function of back azimuth, in 10° increments. (c) Harmonic terms of RFs for $\alpha = 0^\circ$ in equation (1). (d) Amplitude variation of B_{\perp} as a function of α . See □ Figure S6 for a set of models in which the slower anisotropic layer overlays the faster isotropic layer, and corresponding RFs and RFharmonics. The color version of this figure is available only in the electronic edition.



▲ **Figure 4.** Schematics showing three model geometries for RF modeling: (a) isotropic model with four layers without anisotropy, (b) anisotropic mantle lid (AML) model, and (c) anisotropic oceanic crust (AOC) model. We used the velocity model of Phillips *et al.* (2012) and dipping angle of 25° for the dipping oceanic crust. The density of each layer was obtained from Tassara *et al.* (2006). Anisotropy in the anisotropic layer was assumed as hexagonal anisotropy with fast-axis symmetry; its strength and orientation are listed in Tables 2 and 3. See ◎ Figure S8 for models involving an ultra-slow layer. The color version of this figure is available only in the electronic edition.

RF RESULTS

We first present single-station RF stacks for two quality stations, PG10 and PE03 (Fig. 2f,g). R-RFs of both stations showed coherent signals with back azimuth, including positive-amplitude signal arrival at 4–5 s (PG10) and 3–4 s (PE03) after the direct P , indicating a downward increase in velocity at the continental Moho (Fig. 2f,g). R-RFs of station PG10 show a positive-amplitude signal arriving at 10 s, indicating Pds from the oceanic Moho (Fig. 2f). T-RFs showed a polarity flip at 10 s with back azimuth of about 240° and 30°–80° (Fig. 2f). R-RFs of station PE03 showed a negative-amplitude signal 6–7 s after the direct P , likely associated with Pds from the top plate interface, and a positive-amplitude signal at 6.5–8 s for the oceanic Moho (Fig. 2g). T-RFs showed a polarity flip at 6.5–8 s with back azimuth of 180°–210° and 40° (Fig. 2g). The observed harmonic moveout of the first P arrival on the radial component may be due to a near-surface low-velocity structure.

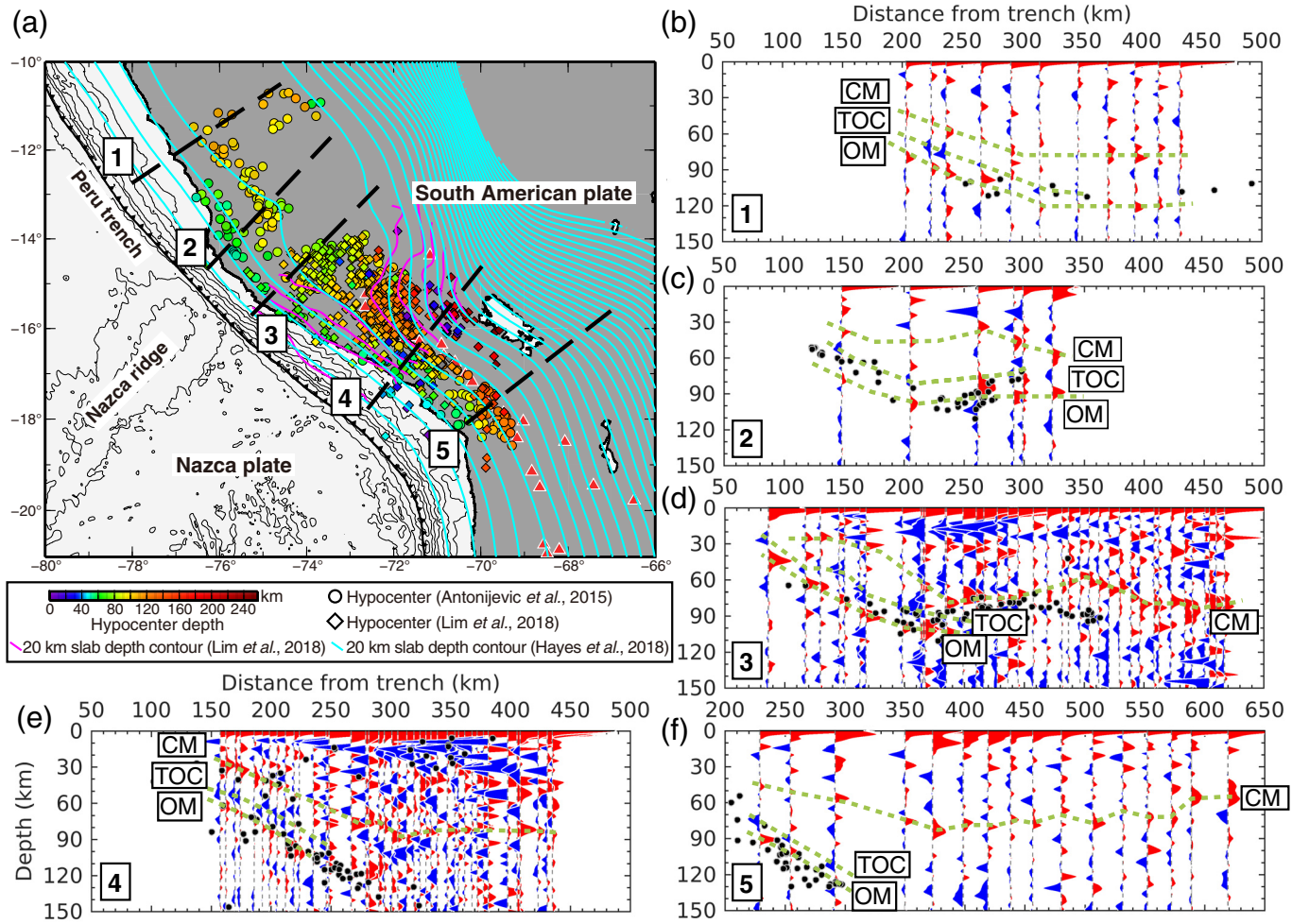
Figure 5b–f shows R-RF images along the five profiles (Figs. 1 and 5a). These images display major seismic discontinuities such as the continental Moho, slab–mantle interface, and oceanic Moho, which we will explain in detail in the Subduction-Zone Structures section. We first describe the isotropic structures of the overall subduction system, derived from all network data (Fig. 5b–f), and later focus on the anisotropic structure obtained from the RF harmonics along profiles 3 and 4 (Fig. 6). These two profiles were selected for harmonic analysis and detailed forward modeling because denser station distribution near the coast is necessary for examining systematic trench-normal changes in the strength and trend of anisotropy (e.g., Song and Kim, 2012a; Audet, 2013).

Subduction-Zone Structures

Flat-Slab Region

Clear negative and positive Pds from the top and bottom interfaces of the subducting oceanic crust were tracked along profiles 1–3, respectively (Fig. 5b–d); these are consistent with previous RF results (Phillips *et al.*, 2012; Phillips and Clayton, 2014; Kim and Clayton, 2015; Ma and Clayton, 2015; Ryan *et al.*, 2016; Bishop *et al.*, 2017). Profiles 2 and 3 traverse the northern and southern edges of the projection of the subducting Nazca ridge (Figs. 1 and 5a). In particular, profile 3 is located at the southern edge of the flat-slab region. The oceanic crust dips from about 20° northwest (Fig. 5b) to about 30° southeast (Fig. 5d). In profile 1, the shallow-dipping top plate interface is clearly imaged until a depth of about 85 km and a lateral distance of 270 km from the trench (Fig. 5b). The flat-lying oceanic Moho is clear at a depth of about 120 km and lateral distance of about 300–440 km from the trench, whereas the upper boundary of the oceanic crust is not (Fig. 5b). In profiles 2 and 3, the shallow-dipping oceanic crust transitions to a roughly flat geometry at a depth of about 80 km and lateral distance of 100 km from the coast (Fig. 5c,d).

We observed noticeable along-arc variation in the depth of the continental Moho in the flat-slab region (Fig. 5b–d), as reported by Bishop *et al.* (2017). Along profile 1, the continental Moho gradually deepens from the coast at a depth of about 45 km, flattening at about 70–80 km and a lateral distance of about 300 km from the trench (Fig. 5b). We observed the shallowest Moho at a depth of 30–50 km, in the middle of profile 2 (Fig. 5c). In profile 3, the continental Moho becomes progressively deeper inland to 55–80 km depth with variable Moho topography, as observed by Ma and Clayton (2015).



▲ Figure 5. Stacked radial RF profile images. (a) Map showing local earthquake locations obtained from Antonijevic *et al.* (2015; colored circles) and Lim *et al.* (2018; colored diamonds), Nazca slab contour (Hayes *et al.*, 2018; Lim *et al.*, 2018), and five trench-perpendicular profiles (1–5) for RFs. (b–f) Stacked radial RFs projected along the five profiles: (b) profile 1 from the FN line, (c) profile 2 from the FM line, (d) profile 3 from the PG line, (e) profile 4 from the PE line, and (f) profile 5 from the CB + CP line. Positive amplitudes (red) indicate increasing impedance with depth; negative amplitudes (blue) indicate increasing impedance with depth. Black dots represent hypocenters determined by (b,c,f) Antonijevic *et al.* (2015) and (d,e) Lim *et al.* (2018). Converted arrivals from the continental Moho (CM), top of the subducting oceanic crust (TOC), and oceanic Moho (OM) are highlighted as green dashed lines in (b–f). The color version of this figure is available only in the electronic edition.

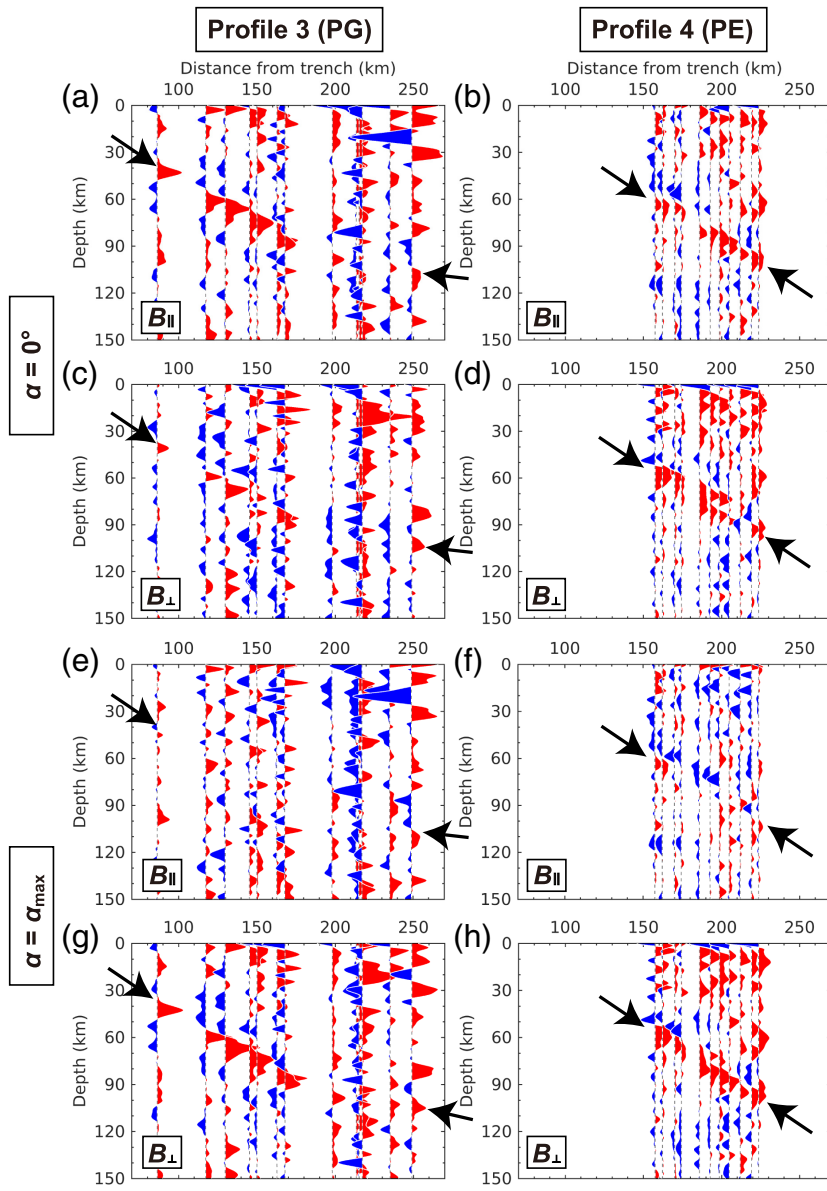
Normal Dip-Slab Region

Clear P_{ds} arrivals from the shallow-dipping oceanic crust were traced along profiles 4 and 5 south of the ridge axis (Fig. 5e,f). In profile 4, a negative and positive pulse pair indicative of the subducting oceanic crust was visible at a lateral distance of about 250 km from the trench and to a depth of about 100 km (Fig. 5e). However, their amplitudes are slightly weaker than those observed for the flat slab (Fig. 5b–d). In profile 5, the oceanic crust was clearly imaged until a depth of about 110 km and a lateral distance of about 300 km from the trench. We observed variation in continental Moho depth in the normal dip-slab region (Fig. 5e,f), as reported by Phillips *et al.* (2012) and Ryan *et al.* (2016). The continental Moho depth in profile 4 gradually deepened from the coast and flattened at a depth of about 80 km and lateral distances of >300 km

from the trench (Fig. 5e). In profile 5, the continental Moho was observed at a depth of about 85 km and lateral distance of about 370 km from the trench (Fig. 5f).

RF Harmonic Decomposition

Figure 6a–d shows the B_{\parallel} and B_{\perp} terms of the first-order harmonics ($k = 1$) when $\alpha = 0^\circ$ for the subset of PG and PE stations (Fig. 1a, white-outlined squares). We observed major P_{ds} conversions in the A term, indicating velocity jumps across interfaces such as the continental Moho and the top and bottom interfaces of the oceanic crust (Fig. S4a,b), as also observed from the R-RFs (Fig. 5d,e). Positive-arrival signals for the oceanic Moho were stronger in the flat-slab region than in the normal dip-slab region (Fig. S4a,b, black dashed lines). B_{\parallel} and B_{\perp} harmonics for both regions showed strong



▲ Figure 6. RF harmonic decomposition for (a–d) $\alpha = 0^\circ$ and (e–h) $\alpha = \alpha_{\max}$ along profiles 3 and 4 (Fig. 5). (a,b,e,f) B_{\parallel} term of the first-order harmonics ($k = 1$). (c,d,g,h) B_{\perp} term of the first-order harmonics ($k = 1$). B terms at the depth of the OM are indicated as black arrows. See (e) Figures S4 and S5 for A and C terms when $\alpha = 0^\circ$ and $\alpha = \alpha_{\max}$, respectively. The color version of this figure is available only in the electronic edition.

and coherent energy at or near the shallow-dipping oceanic crust (Fig. 6a–d, black arrows). In particular, the largest B_{\parallel} amplitudes at the oceanic crust were found in the flat-slab region (Fig. 6a) and the largest B_{\perp} amplitudes were found in the normal dip-slab region (Fig. 6d), suggesting differing preferential orientation at/near the oceanic crust between regions. Although C_{\parallel} and C_{\perp} harmonics also retained some energy near the depth of the subducting oceanic crust, their amplitudes were substantially weaker than those from harmonics of different orders (Fig. S4). Therefore, in this study,

only the A , B_{\parallel} , and B_{\perp} terms were considered in the models to investigate differences in amplitude.

We investigated an angle α_{\max} , which would maximize B_{\perp} amplitude (Table 1; Fig. S3). In the dipping parts of both regions (PG01–PG11 and PE03–PE13; Fig. S2), α_{\max} tended to be confined within a range of 40° (between 280° and 320° , except for a few outliers), whereas in the flat segment (PG15–PG22; Fig. S2), α_{\max} tended to be quite scattered (Table 1; Fig. 7a,b and Fig. S3a). Values of α_{\max} determined for the dipping sections of the two regions were similar to the strike of the subducting plate, mostly parallel to the strike of the trench, which was 310° – 315° (Table 1; Fig. 7a,b and Fig. S3). This result is consistent with our synthetic results from model 1 (Fig. 3), demonstrating that α_{\max} is the strike of the dipping layer.

Figure 6e–h shows the B_{\parallel} and B_{\perp} terms of the first-order harmonics ($k = 1$), when $\alpha = \alpha_{\max}$. Changes in α do not affect the A terms, but change the B and C terms (Fig. S5). At α_{\max} , the amplitude of B_{\perp} at the oceanic Moho is maximized (Fig. 6g,h), whereas that of B_{\parallel} is minimized (Fig. 6e,f). In particular, B_{\perp} amplitude is stronger in the shallow-dipping section (PG01–PG11) of the flat-slab region than in the normal dip-slab region (Fig. 6g,h). Relatively weak amplitudes are expected for the flat segment of the flat-slab region because B_{\perp} amplitude is predominantly controlled by anisotropy. To fully explain the strong B_{\perp} amplitude observed in this study, we next conducted forward modeling of RFs and harmonic decomposition using candidate models, based on previous studies (Fig. 4).

FORWARD-MODELING RESULTS

Figure 8 shows synthetic RF harmonics for three models, to explain observed RF harmonics when $\alpha = \alpha_{\max}$, especially the strong positive amplitude in B_{\perp} terms for the oceanic Moho (Fig. 6g,h; see Figs. S9 and S10 for A and C terms). The best-fitting model parameters for each model (Fig. 4) are listed in Tables 2 and 3. We found that 10% or 20% anisotropy in either the oceanic crust or uppermost mantle layer was critical for minimizing the misfit between the synthetics and the data. A dipping ultra-slow layer (USL) atop the slab did not significantly improve the fit between the synthetics and the data (see the supplemental content to this article for details).

Table 2
Best-Fitting Model Parameters for PG Stations

Station	Isotropic Model			AML			AOC		
	M	Anisotropy (%)	Tr (°)	PI (°)	M	Anisotropy (%)	Tr (°)	PI (°)	M
PG01	1.830	20	0	40	1.452	20	200	60	1.355
PG05	1.230	20	20	50	0.791	20	220	50	0.804
PG06	1.348	20	0	50	0.779	20	200	50	0.929
PG07	0.880	20	0	40	0.466	20	200	60	0.486
PG08	0.732	20	20	40	0.499	20	200	50	0.369
PG10	1.304	20	30	40	1.169	20	230	50	0.901
PG11	0.994	20	20	60	0.706	20	220	50	0.636
PG15	0.822	20	330	50	0.428	20	140	70	0.598
PG16	1.565	20	150	30	1.242	20	290	80	1.150
PG17	0.881	20	280	60	0.619	20	120	80	0.652
PG18	1.148	20	140	30	0.824	20	290	80	0.810
PG21	0.736	20	270	30	0.475	20	130	60	0.421
PG22	1.096	20	120	40	0.801	20	220	60	0.735

AOC, anisotropic oceanic crust model; AML, anisotropic mantle lid model; M, root mean square misfit; PI, plunge of fast axis of symmetry; Tr, trend of fast axis of symmetry.

Table 3
Best-Fitting Model Parameters for PE Stations

Station	Isotropic Model			AML			AOC		
	M	Anisotropy (%)	Tr (°)	PI (°)	M	Anisotropy (%)	Tr (°)	PI (°)	M
PE03	0.842	20	40	60	0.675	20	240	40	0.415
PE04	0.498	20	80	10	0.392	10	280	50	0.396
PE05	0.704	10	350	20	0.492	10	210	30	0.433
PE06	0.158	10	340	10	0.118	10	0	0	0.096
PE07	0.490	20	80	20	0.444	10	270	60	0.411
PE08	0.488	10	110	20	0.468	10	260	10	0.477
PE09	0.374	10	80	30	0.325	20	270	20	0.285
PE10	0.429	20	0	30	0.387	20	210	60	0.450
PE11	0.677	20	30	50	0.426	20	200	70	0.525
PE12	0.645	20	20	50	0.386	20	220	50	0.362
PE13	0.353	20	60	20	0.278	20	250	60	0.267

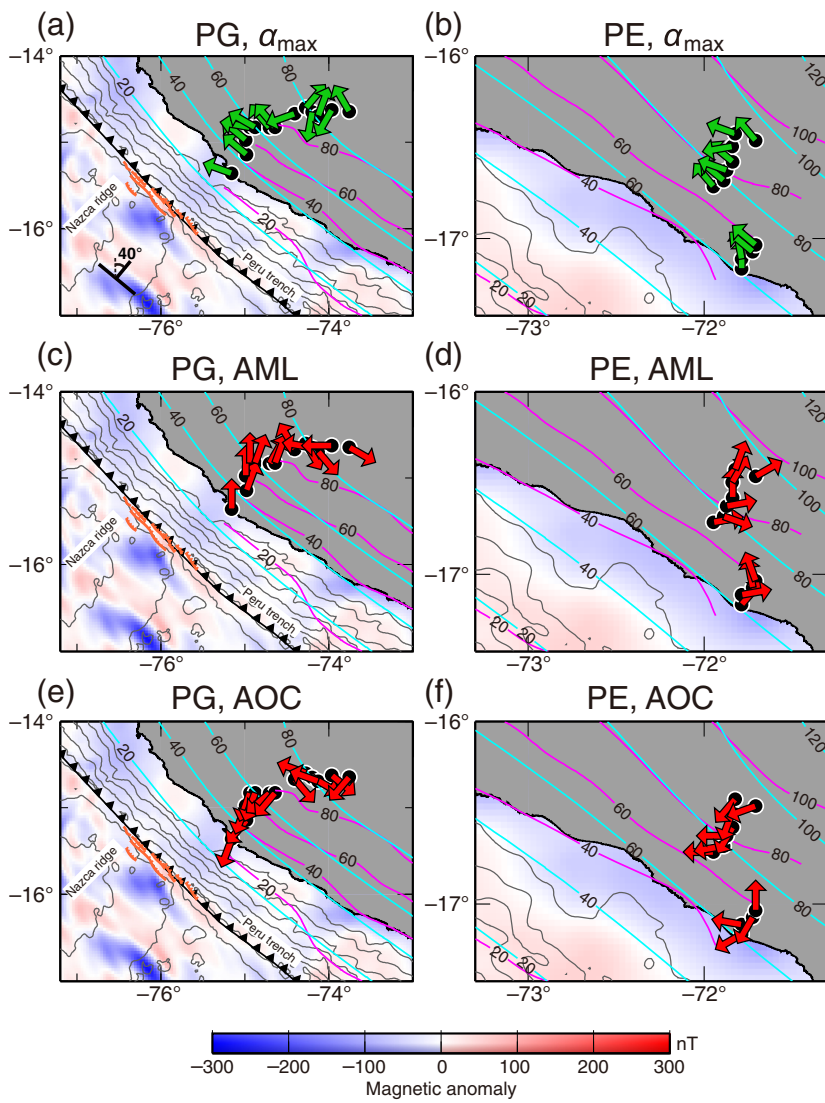
AOC, anisotropic oceanic crust model; AML, anisotropic mantle lid model; M, root mean square misfit; PI, plunge of fast axis of symmetry; Tr, trend of fast axis of symmetry.

Flat-Slab Region

As Figure 8a and ⊕ Figure S9a show, the isotropic model with dipping oceanic crust did not fully explain the strong positive amplitude observed at the oceanic Moho for the A and B_{\perp} terms. For all 13 stations, we found that 20% anisotropy in either the AML or AOC model contributed to this strong B_{\perp} amplitude at depth, and also improved the total misfit of $A + B_{\parallel} + B_{\perp}$ compared with the isotropic model (Fig. 8; Table 2). In summary, the AML model provided the best fit for the observed data for five stations (PG05, PG06, PG07, PG15, and PG17; Table 2), whereas the AOC model provided

the best fit for the other eight stations (PG01, PG08, PG10, PG11, PG16, PG18, PG21, and PG22; Table 2).

Models with an anisotropic layer (Fig. 4b,c) show different dominant fast-axis trends between dipping and flat segments (Fig. 7c,e; Table 2). In the AML model, the fast-axis trend was mainly from the north to northeast (0°–30°) in the dipping segment (Fig. 7c; Table 2). However, in the flat segment, its trend varied directionally, and four stations (PG15, PG16, PG18, and PG22) showed trends aligned subparallel to the 80-km-isodepth contour of the slab models (Fig. 7c). The remaining two stations (PG17 and PG21) were best modeled



▲ Figure 7. Model summary for the (a,c,e) PG and (b,d,f) PE lines. (a,c,e) α_{\max} and trend of the fast symmetry axis in the flat-slab region. (b,d,f) α_{\max} and trend of the fast symmetry axis in the normal dip-slab region. Cyan and pink lines in (a–f) represent 20 km slab contours obtained from Hayes *et al.* (2018) and Lim *et al.* (2018), respectively. Green arrows in (a,b) indicate α_{\max} ; red arrows in (c–f) indicate the trend of fast-axis symmetry determined for each station. Offshore magnetic lineation (Maus *et al.*, 2009) is shown in all panels, and the expected orientations of fossil slab fabric and paleospreading direction are indicated as a black solid bar in (a). Orange lines in (a,c,e) indicate the locations of offshore normal faults with trench-parallel strikes, obtained from a multichannel seismic survey by Hampel *et al.* (2004). The color version of this figure is available only in the electronic edition.

with a west-dipping trend (280° and 270°). Plunge was estimated at 40° – 60° in the dipping segment and 30° – 60° in the flat segment (Table 2).

In the AOC model, the trend for stations in the dipping segment was consistently toward the southwest (200° – 230°), whereas in the flat segment the trend appeared to be quite variable (Fig. 7e). Three stations in the flat segment showed southeast trends (120° , 130° , and 140°), two stations showed a northwest trend (290°), and the last station in the PG line

showed a southwest trend (220° ; Fig. 7e). Five of the six stations in the flat segment showed trend aligned subparallel to the 80-km-isodepth contour of the slab models (Hayes *et al.*, 2018; Lim *et al.*, 2018). Plunge was estimated at 50° – 60° in the dipping segment and 60° – 80° in the flat segment (Table 2).

Normal Dip-Slab Region

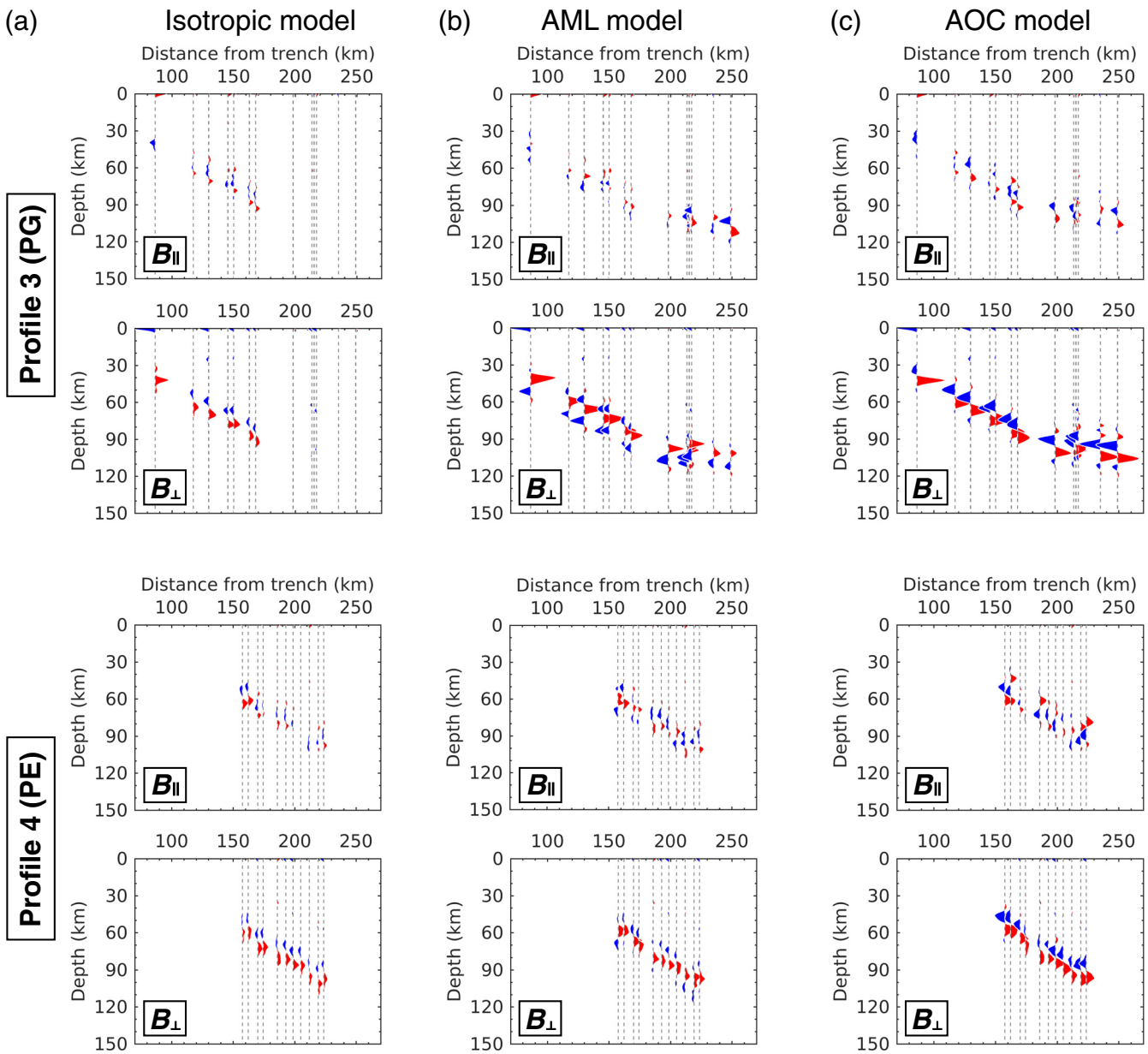
Similar to the flat-slab region, the 10%–20% anisotropy reduced the misfit of $A + B_{\parallel} + B_{\perp}$ between the data and synthetics compared with other isotropic models, for all 11 stations in this region (Table 3). The AML model provided the best fit to the observations for four stations (PE04, PE08, PE10, and PE11), and the AOC model for seven stations (PE03, PE05, PE06, PE07, PE09, PE12, and PE13; Table 3). Similar to the flat-slab region, the trends obtained from the AML and AOC models generally pointed in opposite directions, with a 140° – 210° difference (Table 3, except for one station [PE06]). The AML model provided a trend aligned between north and east (340° – 110°) and plunge of 10° – 60° (Fig. 7d; Table 3). The AOC model provided a trend of 200° – 280° and variable plunge of 10° – 70° for 10 stations (excluding PE06) in the normal dip-slab region (Fig. 7f; Table 3).

DISCUSSION

Limiting Factors in Model Resolution

RF modeling to determine anisotropic model parameters is subject to strong trade-offs between isotropic structure, and anisotropy strength and geometry; thus, the models presented in this study are not unique. Typically, such modeling requires assumptions about the symmetry and geometry of the anisotropy to reduce the number of free parameters. Similar trade-offs occur between dip and velocity when trying to solve a heterogeneous isotropic structure. In this study, to reduce the number of parameters, we attempted to fit only large observed amplitudes at the oceanic Moho, and therefore only a limited number of candidate models were considered to fit observed signals along the two profiles.

Therefore, major uncertainty is expected if a fixed layer thickness and velocity contrast are used across the interfaces. Laterally variable material properties along the profile cannot be fully represented by a simple 1D velocity model. As we demonstrated with the USL (see the \oplus supplemental content to this article), a more sophisticated model (e.g., \oplus Fig. S8) may improve the fit of our data over most of the flat-slab region, as well as some localized areas in the normal dip-slab region. To reduce the number of parameters, we set V_S and V_P/V_S



▲ **Figure 8.** Synthetic RF harmonic decomposition for $\alpha = \alpha_{\max}$ along profile 3 (PG01–PG22) and profile 4 (PE03–PE13) using the three models (Fig. 4). The locations of the subset of PG and PE stations are shown as white-outlined squares in Figure 1a. Two harmonic terms (B_{\parallel} and B_{\perp}) were plotted for the best-fitting (a) isotropic four-layer model, (b) the AML model, and (c) the AOC model. See ◎ Figures S9 and S10 for harmonic terms (A , B_{\parallel} , B_{\perp} , C_{\parallel} , and C_{\perp}) of the five models for profiles 3 and 4 (Fig. 4 and ◎ Fig. S8), respectively. The color version of this figure is available only in the electronic edition.

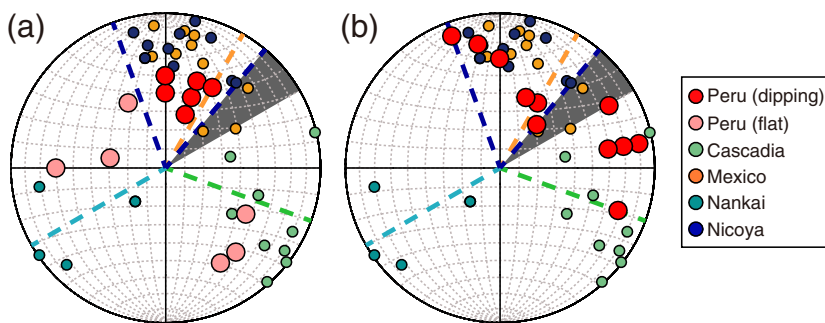
of the USL to 3.4 km/s and 1.75, respectively. However, more realistic values, such as $V_S = 3.3\text{--}3.8$ km/s and $V_P/V_S = 1.64\text{--}2.03$ in the USL of the flat-slab region (Kim and Clayton, 2015) might be necessary to better represent this complex structure.

Previous studies demonstrated the importance of the anisotropic parameter η to seismic signatures (Kawakatsu *et al.*, 2015; Xie *et al.*, 2015; Kawakatsu, 2016) and the empirical scaling relationships between η and anisotropy (Brownlee *et al.*, 2017). Modeling with different η -values such as 0.4–1.1 (Song

and Kim, 2012b) can help improve the fit between the data and synthetics for smaller anisotropy strength (<20%). We also note that the results from a small number of PE stations farthest inland might be slightly biased because P -to- S piercing points at the oceanic Moho (>90 km) partly overlap between the neighboring stations.

AML

Audet (2013) suggested that the AML is a ubiquitous feature of the oceanic upper mantle that preserves its fossil slab fabric



▲ Figure 9. Stereonet figures showing the orientation of the fast axis of AML in the (a) Peruvian flat-slab region (profile 3) and (b) normal dip-slab region (profile 4) in comparison with measurements from other shallow subduction-zone fore-arcs (Audet, 2013). Gray-shaded areas correspond to paleospreading directions for Peru, which are 40°–60° (decreasing value toward the coast; Maus et al., 2009) and were measured perpendicular to offshore magnetic lineations. Colored dashed lines correspond to paleospreading directions for other subduction zones (Audet, 2013). Red and pink circles represent stations that sample dipping and flat segments, respectively, along the PG line. The color version of this figure is available only in the electronic edition.

and paleospreading directions. This fabric is considered to form at the midocean ridge when olivine crystals align with the direction of plate spreading. AML has been identified at young (<25 Ma) subducting slabs in Cascadia, Nankai, Mexico, and Nicoya, with variable thickness and anisotropy strength (Audet, 2013). In these regions, fast-axis trends were found to be mainly within <20° of the fossil spreading direction (Audet, 2013). The strong B_{\perp} amplitudes observed in this study (Fig. 6g,h) require an AML with the 10%–20% anisotropy in both the flat and normal dip-slab regions of southern Peru.

In the dipping segment of the flat-slab region, the fast symmetry axes showed consistent north–northeast trends (at 0°, 20°, and 30°; Fig. 7c); these occurred in the northward direction from the fossil spreading axis, which was about 40°–60° measured from offshore magnetic lineation (Maus et al., 2009; Fig. 9a). The observed north–south orientation of fast-axis directions at depths <80 km is consistent with shear-wave splitting data, which showed strike-parallel (roughly north–south) slab anisotropy at a depth of 200–400 km in the flat-to-normal slab-dip transition zone (Eakin, Long, Scire, et al., 2015). A dominant trench-normal trend of the fast symmetry axis may point to the presence of frozen olivine fabric in the uppermost mantle of the slab, in alignment with the direction of paleoplate spreading. To date, both the age and depth of the AML in southern Peru are the greatest among subduction zones identified for the AML (Audet, 2013).

The coherent direction observed for the north–northeast fast-axis trend drastically changed as the slab flattened at a depth of about 80 km (Fig. 7c). Such seismic changes in the flat-slab segment pattern were also observed by previous studies utilizing shear-wave splitting and surface-wave constraints (Eakin, Long, Scire, et al., 2015; Antonijevic et al., 2016). This disrupted trend pattern may indicate deformation of slab fabric due to a high degree of mechanical coupling between the

two plates, as well as interaction with the Nazca ridge during the slab-flattening process (Espurt et al., 2008). Unlike the trend, the plunge did not show any abrupt change in the flat-slab segment (Table 2).

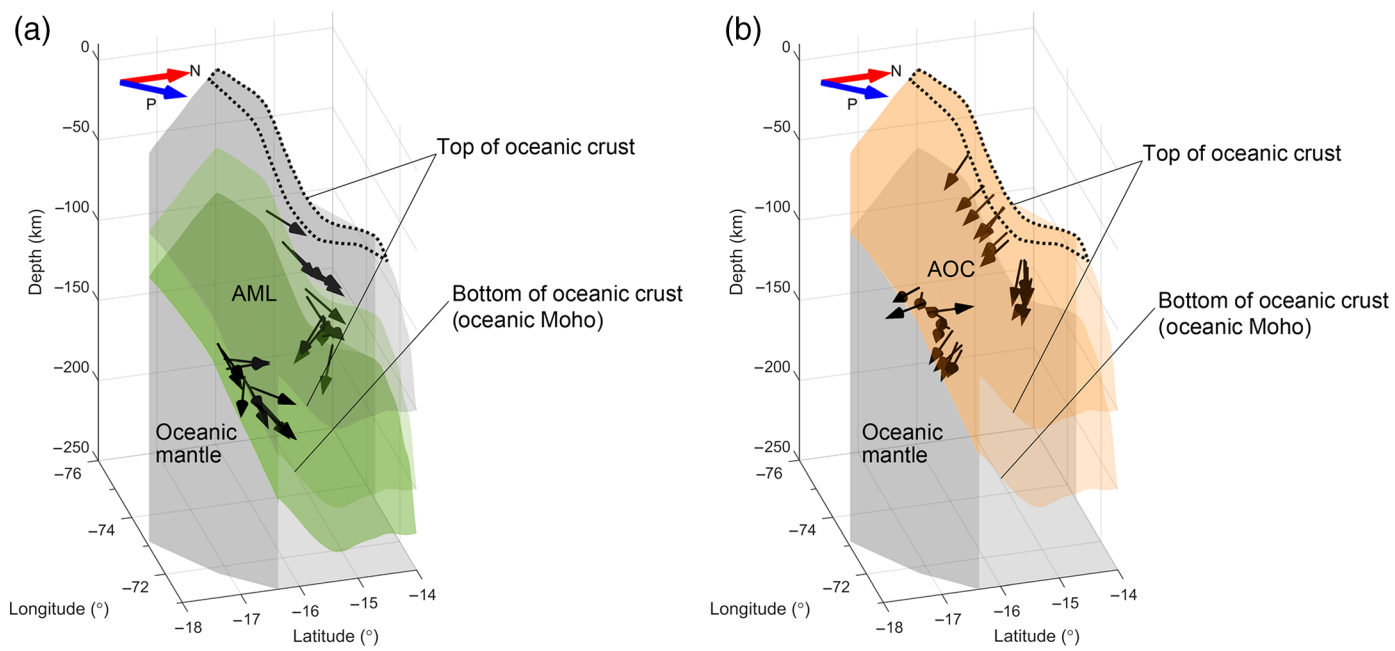
In the normal dip-slab region, south of the ridge axis, fast-axis trends were mainly between north and east (Fig. 7d). Figure 10a shows 3D image of the fast symmetry axis orientation, including both trend and plunge, for the AML best-fit model. Near the coast, we found trends with ≤20° deviation from the fossil spreading axis. However, farther inland, their values were greatly scattered with respect to the fossil spreading axis, with five showing fast axes trending north–northeast (at 340°, 350°, 0°, 20°, and 30°; Fig. 9b). This rotation of the fast axes from trench-normal to north–south in this region southeast of the Nazca ridge was also observed in a previous surface-wave study (Antonijevic et al., 2016).

In addition to the rotated fast-axis trend, the AOC model produced a smaller misfit between the synthetics and data than produced by the AML model in stations with shallow slab depth (PE03, PE05, PE06, and PE07), indicating that localized mantle-lid anisotropy may not be evident at the shallow slab depth of the normal dip-slab region. Anisotropy related to fossil plate motion may have been at least partly overprinted by the tectonic process before subduction but after spreading. Intense tectonic shortening at 42–49.5 Ma associated with rapid convergence (>10 cm/yr) between the Nazca and South American plates (Pardo-Casas and Molnar, 1987) may have had an effect on deformation of slab fossil fabric in the region south of the ridge.

AOC

The strong positive B_{\perp} amplitude observed in the RF harmonics (Fig. 6g,h) can be explained by the AOC model with the 10%–20% anisotropy. As discussed earlier, the AOC model provided the best explanation for the data in the shallow normal dip-slab region. In the dipping segment in both the flat and normal dip-slab regions, fast-axis trends were found to be trench-perpendicular, mostly plunging toward the trench (Fig. 7e,f). In the flat segment, the trend was mostly aligned subparallel to the slab isodepth contour (Hayes et al., 2018; Lim et al., 2018; Fig. 7e), indicating along-strike extension induced by slab flattening (Eakin, Long, Scire, et al., 2015; Kumar et al., 2016). Figure 10b shows 3D image of the fast symmetry axis orientation, including both trend and plunge, for the AOC best-fit model results.

The 10%–20% anisotropy observed in oceanic crust may indicate strong crystal-preferred orientation (CPO) of minerals. Enhanced seismic anisotropy in many subduction zones has been partly attributed to basaltic oceanic crust transforming to blueschist facies rocks (Cao and Jung, 2016). Blueschist facies minerals such as glaucophane, epidote, and phengite typically show strong



▲ Figure 10. 3D image of the anisotropic structure of the southern Peruvian subduction zone obtained by the (a) AML model and the (b) AOC model. The z axis represents the depth of the top of the oceanic crust, and thicknesses of the anisotropic layers (AML and AOC) are exaggerated for the purpose of visualization. Green-shaded layer indicates AML in (a); orange-shaded layer indicates AOC in (b). Red and blue arrows indicate north (N) and paleospreading (P) directions, respectively. Black arrows indicate fast symmetry axis orientations (trend and plunge) within each anisotropic layer. Top and bottom interfaces of the oceanic crust are indicated. Slab geometry was obtained from Lim *et al.* (2018); dotted black line indicates the subducting Nazca ridge. This image is a snapshot image of the movie at a view azimuth of 74°. See Movies S1 and S2 for full 3D images at a view azimuth between 0° and 360°. The color version of this figure is available only in the electronic edition.

seismic anisotropy (Ji *et al.*, 2002; Bezacier *et al.*, 2010; Ha *et al.*, 2018); thus, the seismic anisotropy of blueschist facies rocks can be strong ($AV_p = 16.1\%$ and $AV_s = 10.3\%$ for V_p and V_s anisotropy, respectively; Bezacier *et al.*, 2010). A previous study of seismic properties of the Nazca oceanic crust suggested that the dominant mineral phase in the upper oceanic crust was amphibole (Kim and Clayton, 2015). Amphibole-bearing oceanic crust has also been reported in the central Andes (21° S; ANCOP Working Group, 2003). These reports support our finding of strong seismic anisotropy within oceanic crust. In addition, bending-related faults offshore of Peru (Fig. 7e; Hampel *et al.*, 2004) have been shown to induce seismic anisotropy within the uppermost portion of the subducting plate by CPO formation of hydrous minerals within the faults (Faccenda *et al.*, 2008). CPO of hydrous minerals produced by alteration (e.g., serpentine, talc, amphibole, and chlorite) may produce strong oceanic crust anisotropy (Mainprice and Ildefonse, 2009). A potential source of seismic anisotropy also includes the presence of ridge-parallel cracks (Almendros *et al.*, 2000).

CONCLUSIONS

Teleseismic RFs provide complementary depth-dependent seismic anisotropy that is difficult to obtain using other types of seismological data (e.g., shear-wave splitting and surface-wave dispersion), because RFs are highly sensitive to the depth of

contrast in anisotropic properties. We constrained the hexagonal anisotropic structure of the upper part of the subducting oceanic Nazca plate along the South American margin at 12°–20° S latitude by analyzing azimuthally varying characteristics of the Pds phases. Harmonic decomposition and forward modeling of RF harmonics supported one of two models, of the AOC or AML below the subducted crust, which includes the 10%–20% anisotropy in the layer with predominant trench-normal fast-axis symmetry for the dipping segment of the slab. Strong mineral texture within the oceanic crust or/and upper oceanic crust due to bending-related faults and the ridge may contribute to such strong anisotropy across southern Peru. Our data also suggest the presence of frozen olivine fabric in alignment with the direction of paleoplate spreading, which is preserved only below the dipping oceanic crust in the flat-slab system. The fossil fabric below the flat-lying crust may have been overprinted by deformation due to strong tectonic coupling between the two plates in response to subduction of the Nazca ridge during the slab-flattening process.

DATA AND RESOURCES

The seismic waveform data analyzed in this study were downloaded using the webservice of the Incorporated Research Institutions for Seismology Data Management Center

(IRIS-DMC; <http://service.iris.edu>, last accessed June 2018). The organizations responsible for deploying the temporary and permanent seismic networks in southern Peru are listed under network-specific links. ☐

ACKNOWLEDGMENTS

The authors acknowledge support from the Creative Pioneering Researchers Program of Seoul National University (SNU SRnD 3345-20160014), and the Nuclear Safety Research Program through the Korea Foundation of Nuclear Safety (KoFONS), granted financial resource from the Nuclear Safety and Security Commission (NSSC), Republic of Korea (Number 1705010). The authors are grateful to the many institutions that deployed and maintained temporary networks in southern Peru. In particular, the authors thank the Peru Subduction Experiment (PeruSE) for providing the seismic waveform data used in this study. Seismic instruments for the Central Andean Uplift and Geodynamics of High Topography (CAUGHT) and the Peru Lithosphere and Slab Experiment (PULSE) experiments were provided by the Incorporated Research Institutions for Seismology (IRIS) through the Program for the Array Seismic Studies of the Continental Lithosphere (PASSCAL) Instrument Center at the New Mexico Institute of Mining and Technology. The IRIS Consortium facilities are supported by the National Science Foundation (NSF) under Cooperative Agreement EAR-1261681 and the Department of Energy (DOE) National Nuclear Security Administration. The Global Seismographic Network (GSN) NNA station is a cooperative scientific facility operated jointly by the IRIS, the U.S. Geological Survey (USGS), and the NSF, under Cooperative Agreement EAR-1261681. Finally, the authors thank Editor-in-Chief Zhigang Peng and the two reviewers for their comments and suggestions, which greatly improved this article.

REFERENCES

- Almendros, J., A. H. Barclay, W. S. Wilcock, and G. Purdy (2000). Seismic anisotropy of the shallow crust at the Juan de Fuca ridge, *Geophys. Res. Lett.* **27**, 3109–3112.
- Ammon, C. J. (1991). The isolation of receiver effects from teleseismic *P* waveforms, *Bull. Seismol. Soc. Am.* **81**, 2504–2510.
- ANCORP Working Group (2003). Seismic imaging of a convergent continental margin and plateau in the central Andes (Andean Continental Research Project 1996 (ANCORP'96)), *J. Geophys. Res.* **108**, 2328.
- Antonijevic, S. K., L. S. Wagner, S. L. Beck, M. D. Long, G. Zandt, and H. Tavera (2016). Effects of change in slab geometry on the mantle flow and slab fabric in southern Peru, *J. Geophys. Res.* **121**, 7252–7270.
- Antonijevic, S. K., L. S. Wagner, A. Kumar, S. L. Beck, M. D. Long, G. Zandt, H. Tavera, and C. Condori (2015). The role of ridges in the formation and longevity of flat slabs, *Nature* **524**, 212–215.
- Audet, P. (2013). Seismic anisotropy of subducting oceanic uppermost mantle from fossil spreading, *Geophys. Res. Lett.* **40**, 173–177.
- Audet, P. (2015). Layered crustal anisotropy around the San Andreas fault near Parkfield, California, *J. Geophys. Res.* **120**, 3527–3543.
- Bar, N., M. D. Long, L. S. Wagner, S. L. Beck, G. Zandt, and H. Tavera (2019). Receiver function analysis reveals layered anisotropy in the crust and upper mantle beneath southern Peru and northern Bolivia, *Tectonophysics* **753**, 93–110.
- Beck, S., G. Zandt, and L. Wagner (2010). Central Andean uplift and the geodynamics of the high topography, International Federation of Digital Seismography Networks, Dataset/Seismic Network, doi: [10.7914/SN/ZG_2010](https://doi.org/10.7914/SN/ZG_2010).
- Bezacier, L., B. Reynard, J. Bass, J. Wang, and D. Mainprice (2010). Elasticity of glaucophane, seismic velocities and anisotropy of the subducted oceanic crust, *Tectonophysics* **494**, 201–210.
- Bianchi, I., J. Park, N. Piana Agostinetti, and V. Levin (2010). Mapping seismic anisotropy using harmonic decomposition of receiver functions: An application to Northern Apennines, Italy, *J. Geophys. Res.* **115**, no. B12317, doi: [10.1029/2009JB007061](https://doi.org/10.1029/2009JB007061).
- Bishop, B. T., S. L. Beck, G. Zandt, L. Wagner, M. Long, S. K. Antonijevic, A. Kumar, and H. Tavera (2017). Causes and consequences of flat-slab subduction in southern Peru, *Geosphere* **13**, 1392–1407.
- Brownlee, S. J., V. Schulte-Pelkum, A. Raju, K. Mahan, C. Condit, and O. F. Orlandini (2017). Characteristics of deep crustal seismic anisotropy from a compilation of rock elasticity tensors and their expression in receiver functions, *Tectonics* **36**, 1835–1857.
- Cao, Y., and H. Jung (2016). Seismic properties of subducting oceanic crust: Constraints from natural lawsonite-bearing blueschist and eclogite in Sivrihisar massif, Turkey, *Phys. Earth Planet. In.* **250**, 12–30.
- Cassidy, J. (1992). Numerical experiments in broadband receiver function analysis, *Bull. Seismol. Soc. Am.* **82**, 1453–1474.
- Dougherty, S. L., and R. W. Clayton (2015). Seismic structure in southern Peru: Evidence for a smooth contortion between flat and normal subduction of the Nazca plate, *Geophys. J. Int.* **200**, 534–555.
- Eakin, C. M., and M. D. Long (2013). Complex anisotropy beneath the Peruvian flat slab from frequency-dependent, multiple-phase shear wave splitting analysis, *J. Geophys. Res.* **118**, 4794–4813.
- Eakin, C. M., M. D. Long, S. L. Beck, L. S. Wagner, H. Tavera, and C. Condori (2014). Response of the mantle to flat slab evolution: Insights from local *S* splitting beneath Peru, *Geophys. Res. Lett.* **41**, 3438–3446.
- Eakin, C. M., M. D. Long, A. Scire, S. L. Beck, L. S. Wagner, G. Zandt, and H. Tavera (2015). Internal deformation of the subducted Nazca slab inferred from seismic anisotropy, *Nature Geosci.* **9**, 56–59.
- Eakin, C. M., M. D. Long, L. S. Wagner, S. L. Beck, and H. Tavera (2015). Upper mantle anisotropy beneath Peru from SKS splitting: Constraints on flat slab dynamics and interaction with the Nazca ridge, *Earth Planet. Sci. Lett.* **412**, 152–162.
- Esprut, N., F. Funiciello, J. Martinod, B. Guillaume, V. Regard, C. Faccenna, and S. Brusset (2008). Flat subduction dynamics and deformation of the South American plate: Insights from analog modeling, *Tectonics* **27**, no. TC3011, doi: [10.1029/2007TC002175](https://doi.org/10.1029/2007TC002175).
- Faccenna, M., L. Burlini, T. V. Gerya, and D. Mainprice (2008). Fault-induced seismic anisotropy by hydration in subducting oceanic plates, *Nature* **455**, 1097.
- Frederiksen, A., and M. Bostock (2000). Modelling teleseismic waves in dipping anisotropic structures, *Geophys. J. Int.* **141**, 401–412.
- Ha, Y., H. Jung, and L. A. Raymond (2018). Deformation fabrics of glaucophane schists and implications for seismic anisotropy: The importance of lattice preferred orientation of phengite, *Int. Geol. Rev.* **61**, no. 6, 720–737.
- Hampel, A. (2002). The migration history of the Nazca ridge along the Peruvian active margin: A re-evaluation, *Earth Planet. Sci. Lett.* **203**, 665–679.
- Hampel, A., N. Kukowski, J. Bialas, C. Huebscher, and R. Heinbockel (2004). Ridge subduction at an erosive margin: The collision zone of the Nazca ridge in southern Peru, *J. Geophys. Res.* **109**, no. B02101, doi: [10.1029/2003JB002593](https://doi.org/10.1029/2003JB002593).
- Hayes, G. P., G. L. Moore, D. E. Portner, M. Hearne, H. Flamme, M. Furtney, and G. M. Smoczyk (2018). Slab2, a comprehensive subduction zone geometry model, *Science* **362**, 58–61.
- Ji, S., Q. Wang, and B. Xia (2002). *Handbook of Seismic Properties of Minerals, Rocks and Ores*, Polytech. Int. Press, Montreal, Quebec, 630 pp.

- Kawakatsu, H. (2016). A new fifth parameter for transverse isotropy II: Partial derivatives, *Geophys. J. Int.* **206**, 360–367.
- Kawakatsu, H., J.-P. Montagner, and T.-R. A. Song (2015). On DLA's η , *Geol. Soc. Am. Spec. Pap.* **514**, 33–38.
- Kim, Y., and R. W. Clayton (2015). Seismic properties of the Nazca oceanic crust in southern Peruvian subduction system, *Earth Planet. Sci. Lett.* **429**, 110–121.
- Kumar, A., L. S. Wagner, S. L. Beck, M. D. Long, G. Zandt, B. Young, H. Tavera, and E. Minaya (2016). Seismicity and state of stress in the central and southern Peruvian flat slab, *Earth Planet. Sci. Lett.* **441**, 71–80.
- Ligorria, J. P., and C. J. Ammon (1999). Iterative deconvolution and receiver-function estimation, *Bull. Seismol. Soc. Am.* **89**, 1395–1400.
- Lim, H., Y. Kim, R. W. Clayton, and C. H. Thurber (2018). Seismicity and structure of Nazca plate subduction zone in southern Peru, *Earth Planet. Sci. Lett.* **498**, 334–347.
- Liu, Z., J. Park, and D. M. Rye (2015). Crustal anisotropy in northeastern Tibetan plateau inferred from receiver functions: Rock textures caused by metamorphic fluids and lower crust flow? *Tectonophysics* **661**, 66–80.
- Ma, Y., and R. W. Clayton (2015). Flat slab deformation caused by interplate suction force, *Geophys. Res. Lett.* **42**, 7064–7072.
- Mainprice, D., and B. Ildefonse (2009). Seismic anisotropy of subduction zone minerals—Contribution of hydrous phases, in *Subduction Zone Geodynamics*, S. Lallemand and F. Funiciello (Editors), Springer, Berlin-Heidelberg, Germany, 63–84.
- Maus, S., U. Barckhausen, H. Berkenbosch, N. Bournas, J. Brozena, V. Childers, F. Dostaler, J. D. Fairhead, C. Finn, R. R. B. von Frese, et al. (2009). EMAG2: A 2-arc min resolution earth magnetic anomaly grid compiled from satellite, airborne, and marine magnetic measurements, *Geochem. Geophys. Geosys.* **10**, no. Q08005, doi: [10.1029/2009GC002471](https://doi.org/10.1029/2009GC002471).
- Müller, R. D., M. Sdrolias, C. Gaina, and W. R. Roest (2008). Age, spreading rates, and spreading asymmetry of the world's ocean crust, *Geochem. Geophys. Geosys.* **9**, no. Q04006, doi: [10.1029/2007GC001743](https://doi.org/10.1029/2007GC001743).
- Nagaya, M., H. Oda, H. Akazawa, and M. Ishise (2008). Receiver functions of seismic waves in layered anisotropic media: Application to the estimate of seismic anisotropy, *Bull. Seismol. Soc. Am.* **98**, 2990–3006.
- Norabuena, E., L. Leffler-Griffin, A. Mao, T. Dixon, S. Stein, I. S. Sacks, L. Ocola, and M. Ellis (1998). Space geodetic observations of Nazca–South America convergence across the central Andes, *Science* **279**, 358–362.
- Pardo-Casas, F., and P. Molnar (1987). Relative motion of the Nazca (Farallon) and South American plates since Late Cretaceous time, *Tectonics* **6**, 233–248.
- Park, J., and V. Levin (2016). Anisotropic shear zones revealed by backazimuthal harmonics of teleseismic receiver functions, *Geophys. J. Int.* **207**, 1216–1243.
- Peru Subduction Experiment (PeruSE) (2013). Peru subduction experiment, *Caltech*, Dataset, doi: [10.7909/C3H41PBZ](https://doi.org/10.7909/C3H41PBZ).
- Phillips, K., and R. W. Clayton (2014). Structure of the subduction transition region from seismic array data in southern Peru, *Geophys. J. Int.* **196**, 1889–1905.
- Phillips, K., R. W. Clayton, P. Davis, H. Tavera, R. Guy, S. Skinner, I. Stubailo, L. Audin, and V. Aguilar (2012). Structure of the subduction system in southern Peru from seismic array data, *J. Geophys. Res.* **117**, no. B11306, doi: [10.1029/2012JB009540](https://doi.org/10.1029/2012JB009540).
- Piana Agostinetti, N., and M. S. Miller (2014). The fate of the down-going oceanic plate: Insight from the northern Cascadia subduction zone, *Earth Planet. Sci. Lett.* **408**, 237–251.
- Piana Agostinetti, N., I. Bianchi, A. Amato, and C. Chiarabba (2011). Fluid migration in continental subduction: The Northern Apennines case study, *Earth Planet. Sci. Lett.* **302**, 267–278.
- Porter, R., G. Zandt, and N. McQuarrie (2011). Pervasive lower-crustal seismic anisotropy in southern California: Evidence for underplated schists and active tectonics, *Lithosphere* **3**, 201–220.
- Rondenay, S. (2009). Upper mantle imaging with array recordings of converted and scattered teleseismic waves, *Surv. Geophys.* **30**, 377–405.
- Ryan, J., S. Beck, G. Zandt, L. Wagner, E. Minaya, and H. Tavera (2016). Central Andean crustal structure from receiver function analysis, *Tectonophysics* **682**, 120–133.
- Schulte-Pelkum, V., and K. H. Mahan (2014a). Imaging faults and shear zones using receiver functions, *Pure Appl. Geophys.* **171**, 2967–2991.
- Schulte-Pelkum, V., and K. H. Mahan (2014b). A method for mapping crustal deformation and anisotropy with receiver functions and first results from USArray, *Earth Planet. Sci. Lett.* **402**, 221–233.
- Scire, A., G. Zandt, S. Beck, M. Long, L. Wagner, E. Minaya, and H. Tavera (2015). Imaging the transition from flat to normal subduction: Variations in the structure of the Nazca slab and upper mantle under southern Peru and northwestern Bolivia, *Geophys. J. Int.* **204**, 457–479.
- Shioi, K., and J. Park (2008). Structural features of the subducting slab beneath the Kii Peninsula, central Japan: Seismic evidence of slab segmentation, dehydration, and anisotropy, *J. Geophys. Res.* **113**, no. B10318, doi: [10.1029/2007JB005535](https://doi.org/10.1029/2007JB005535).
- Song, T.-R. A., and Y. Kim (2012a). Anisotropic uppermost mantle in young subducted slab underplating Central Mexico, *Nature Geosci.* **5**, 55–59.
- Song, T.-R. A., and Y. Kim (2012b). Localized seismic anisotropy associated with long-term slow-slip events beneath southern Mexico, *Geophys. Res. Lett.* **39**, L09308, doi: [10.1029/2012GL051324](https://doi.org/10.1029/2012GL051324).
- Tassara, A., H.-J. Götz, S. Schmidt, and R. Hackney (2006). Three-dimensional density model of the Nazca plate and the Andean continental margin, *J. Geophys. Res.* **111**, no. B0940, doi: [10.1029/2005JB003976](https://doi.org/10.1029/2005JB003976).
- Wagner, L., S. Beck, and M. Long (2010). PerU lithosphere and slab experiment, International Federation of Digital Seismography Networks, Dataset/Seismic Network, doi: [10.7914/SN/ZD_2010](https://doi.org/10.7914/SN/ZD_2010).
- Ward, K. M., G. Zandt, S. L. Beck, L. S. Wagner, and H. Tavera (2016). Lithospheric structure beneath the northern Central Andean plateau from the joint inversion of ambient noise and earthquake-generated surface waves, *J. Geophys. Res.* **121**, 8217–8238.
- Weiss, T., S. Siegesmund, W. Rabbel, T. Bohlen, and M. Pohl (1999). Seismic velocities and anisotropy of the lower continental crust: A review, *Pure Appl. Geophys.* **156**, 97–122.
- Xie, J., M. H. Ritzwoller, S. Brownlee, and B. Hacker (2015). Inferring the oriented elastic tensor from surface wave observations: Preliminary application across the western United States, *Geophys. J. Int.* **201**, 996–1021.

*Hyunsun Kang
YoungHee Kim
School of Earth and Environmental Sciences
Seoul National University
Seoul 08826
Republic of Korea
hyunsun91@snu.ac.kr
younghkim@snu.ac.kr*

Published Online 1 May 2019